Hydrologic Dynamics of the Ground-Water-Dependent Sian Ka'an Wetlands, Mexico, Derived from InSAR and SAR Data

Bibi R. N. Gondwe · Sang-Hoon Hong ·
Shimon Wdowinski · Peter Bauer-Gottwein

Abstract The 5,280 km^2 Sian Ka'an Biosphere Reserve includes pristine wetlands fed by ground water from the karst aquifer of the Yucatan Peninsula, Mexico. The inflow through underground karst structures is hard to observe making it difficult to understand, quantify, and predict the wetland dynamics. Remotely sensed Synthetic Aperture Radar (SAR) amplitude and phase observations offer new opportunities to obtain information on hydrologic dynamics useful for wetland management. Backscatter amplitude of SAR data can be used to map flooding extent. Interferometric processing of the backscattered SAR phase data (InSAR) produces temporal phase-changes that can be related to relative water level changes in vegetated wetlands. We used 56 RADARSAT-1 SAR acquisitions to calculate 38 interferograms and 13 flooding maps with 24 day and 48 day time intervals covering July 2006 to March 2008. Flooding extent varied between 1,067 km^2 and 2,588 km^2 during the study period, and main water input was seen to take place in sloughs during October–December. We propose that main water input areas are associated with water-filled faults that transport ground water from the catchment to the wetlands. InSAR and Landsat data revealed local-scale water divides and surface water flow directions within the wetlands.

Introduction

The 5,280 km^2 Sian Ka'an Biosphere Reserve (RBSK) is both a UNESCO World Heritage and Ramsar site, thus recognized to be internationally important. Located on Mexico's Caribbean coast (Fig. 1) it is one of the largest protected areas in Mexico. The area supports tropical forests, coral reefs, coastal savannahs, swamps, marshes, and mangroves, with a rich biodiversity and both endemic and endangered species (Pozo de la Tijera and Escobedo Cabrera 1999; Lopez-Ornat and Ramo 1992). Approximately one third of the area consists of wetlands in a mosaic of freshwater sloughs, channels, floodplains, and brackish tidally influenced areas. The Sian Ka'an wetlands provide protection from the impact of hurricanes and storms to the inland areas. In addition, their recreational value is increasingly being recognized by the tourism industry in the surrounding areas.

Ground water from the karst aquifer of the Yucatan Peninsula feeds the Sian Ka'an wetlands. The inflow through underground cave systems and karst structures is not directly observable making it difficult to understand, quantify, and predict the wetland dynamics. Yet, understanding the hydrology of the wetland is important for management of its water resources and for protecting the aquatic ecosystems. This is crucial as the wetland's catchment is under pressure from rapidly developing tourism activities, and intensifying agricultural and urban development (Mazzotti et al. 2005).

Space-based synthetic aperture radar (SAR) data offer possibilities for monitoring and analyzing the hydrologic

B. R. N. Gondwe (✉) · P. Bauer-Gottwein
Department of Environmental Engineering,
Technical University of Denmark,
Miljoevej, Building 113,
DK-2800 Kgs. Lyngby, Denmark
e-mail: bng@env.dtu.dk

S.-H. Hong · S. Wdowinski
Division of Marine Geology and Geophysics,
University of Miami,
4600 Rickenbacker Causeway,
Miami, FL 33149, USA
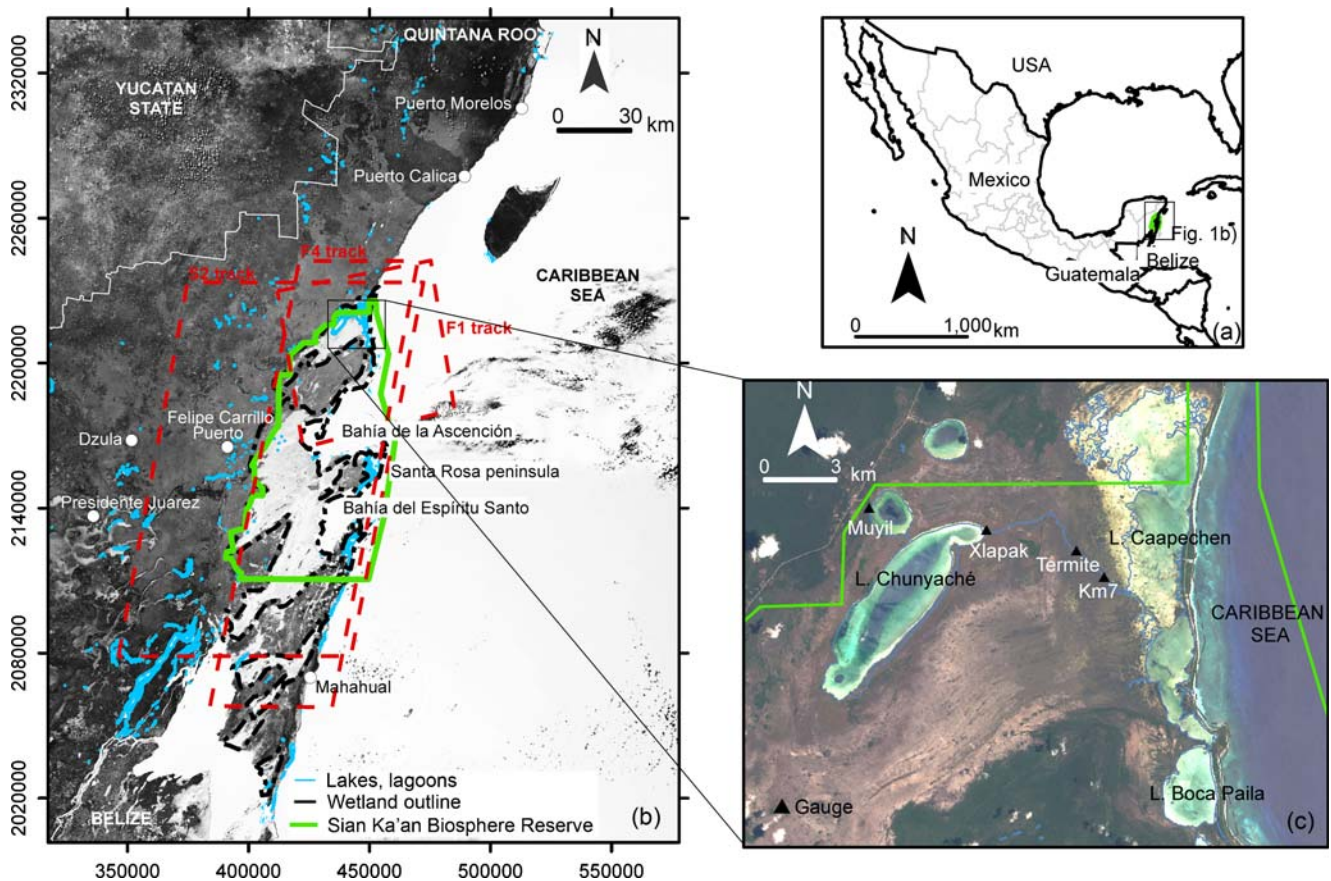
Fig. 1 Location of the study area and sites mentioned in the text. Background of **b** is Landsat TM Tri-Decadal mosaic, band 4 (near-infrared), with reversed color axis so that high absorbance is indicated by *bright colors* and vice versa. Water bodies, having high absorbance

of near-infrared wavelengths, are therefore bright in this image. State and country boundaries are shown with a *thin white line*. Background of **c** is Landsat imagery true color composite (RGB: band 3, 2, 1)

dynamics of wetlands from space. SAR is an active microwave sensor, unaffected by cloud-cover and daylight conditions. It measures two observables of the backscattered signal: amplitude and phase. Both observables are sensitive to wetland hydrologic conditions. Pope et al. (1997) showed that the SAR backscatter from both L-band (wavelength, $\lambda = 24.0$ cm) and C-band ($\lambda = 5.7$ cm) data in a marshy wetland changed in amplitude and phase as the degree of flooding increased. In inundated areas with vegetation protruding through the water surface the radar signal will double-bounce on the water surface and the plants' stems, and thus it is backscattered to the satellite (Richards et al. 1987). The amplitude of radar backscatter depends on the degree of inundation, canopy closure, and canopy height, as these elements modify the dielectric constant of the surface and surface roughness (Ulaby et al. 1996; Bourgeau-Chavez et al. 2005). Temporal changes in the amplitude can thus indicate a change in flooding conditions. The backscatter amplitude's standard deviation also provides information on the degree of flooding in vegetated wetlands. Phase change of radar backscatter can,

on the other hand, be related to changes in the surface water levels of vegetated wetlands using interferometric techniques. If water levels have changed between two image acquisitions, the travel time of the backscattered radar signal will also change (range change), yielding a phase change in an interferogram. The interferometric phase depends on the length of the baseline connecting the position of the satellite antenna at the two different image acquisitions, the topographical relief, the degree of cross-correlation between images for each pixel location (coherence), and the topographic displacement, which can be water level change for a wetland (Alsdorf et al. 2000). Since the first two can be determined with a certain accuracy, the degree of relative displacement may be obtained through SAR interferometry (InSAR) when there is a significant degree of image coherence.

Amplitude of SAR backscatter has previously been used to map flooding extent of wetlands (e.g., Hess et al. 2003; Bourgeau-Chavez et al. 2005; Lang and Kasischke 2008; Sass and Creed 2008). InSAR has been used to analyze hydrodynamics and map centimeter-level changes in Am-

azon floodplains (Alsdorf et al. 2000, 2001, 2007), Everglades wetlands (Wdowinski et al. 2004, 2008; Kim et al. 2005), and Louisiana marshes (Lu et al. 2005; Kim et al. 2005; Lu and Kwoun 2008). InSAR estimates of water level change over wetlands have been found to be accurate within centimeters (Alsdorf et al. 2001, 2007; Wdowinski et al. 2008).

In this paper we use SAR and InSAR data to detect spatio-temporal changes in flooding in Sian Ka'an and analyze flow directions and relative water level changes in the wetlands. We identify locations of main water sources to the wetlands and show in which season main inflow occurs.

Methods

Study Area and Ancillary Data

Sian Ka'an is located in a tropical climate, with distinct wet/dry periods. The rainy season is from May to October, and average precipitation in the catchment ranges from 840 mm/year to 1,550 mm/year (Comisión Nacional del Agua 2008). Most precipitation occurs near the Caribbean coast and in the southern part of Quintana Roo. The area is prone to hurricanes, and Hurricane Dean made landfall in Sian Ka'an on 21 August 2007. Actual evapotranspiration rates are poorly known; estimates range from 40% to 85% of mean annual precipitation (Lesser 1976; Beddows 2004). Recent estimates using remotely sensed data indicate rates in the higher end of this interval (Lerer 2008). Terrain elevations range from 0 m to 20 m above mean sea level (USGS 2006). Because the topographic gradient is very low, small elevation differences determine whether areas are dry land forests, seasonally inundated areas, or permanent wetlands. Vegetation in the Sian Ka'an wetlands consists mainly of perennial sedges and grasses, with mangroves being present in the near-coastal areas (Morales Barbosa 1992).

We installed surface water gauges in Sian Ka'an in early 2007 to obtain in situ data to verify and calibrate InSAR water level change measurements. Gauges were referenced to mean sea level using carrier-phase GPS and manually read. Estimated uncertainty with respect to mean sea level was 1–7 cm based on reoccupation with GPS antennas. Successive readings at the same location had an estimated accuracy of 1 cm on temporal water level variation. Limited accessibility to the wetlands constrained the number of gauges installed to four. All were located in a 1–2 m wide natural channel in the northern part of the reserve, thus representing a limited part of the wetlands (Fig. 1c). Within the monitored time interval, the water level changes in the natural channel were uniform throughout its west-east

direction, and the water level sloped 100–120 cm towards the coastal lagoons over a 10 km stretch, giving a hydraulic gradient of 100–120 ppm here.

Approach

SAR Amplitude Data and Analysis

To map spatio-temporal changes in the degree of flooding we used a single-date parallelepiped image classification approach based on quantitative analysis of pixel backscatter amplitude. Data for this analysis consisted of 13 RADARSAT-1 (C-band, $\lambda = 5.6$ cm) SAR images, Standard Beam track S2 (descending), covering 18 August 2006 to 21 February 2008 (Fig. 2). The generally open and simple vegetation canopies in the Sian Ka'an wetlands enable C-band SAR to penetrate the vegetation. The RADARSAT-1 orbit repeat cycle is 24 days. We chose to use every other of the images available, yielding time steps of 48 days. However, just after Hurricane Dean (September 2007) we used 24 day time steps to resolve the effect of this event in detail. Scenes were cut to display the main wetlands of Sian Ka'an outlined in Fig. 1. Amplitude (σ_0) images were created from Single Look Complex (SLC) β_0 images using look-up tables of each pixel's incidence angle. Due to the flat topography of the study area, topographic effects on σ_0 were considered negligible and hence not corrected for. Images were filtered to reduce the effect of speckle — the inherent multiplicative noise of radar images. We found that applying a Lee filter iteratively using window sizes of 3×3 pixels, then 5×5 and 7×7 pixels gave the best speckle removal while still preserving edges. This method was recommended by Rio and Lozano-García (2000). Filtering was carried out on the intensity of the image (σ_0^2) and thereafter converted back to σ_0 values. Before analysis, σ_0 values were converted to dB. Image resolution after geocoding to UTM (zone 16, WGS84 datum) was 58 m by 61.5 m.

A notable difference in backscatter amplitude was immediately observed for known wetland and non-wetland areas. Since radar backscatter varies with degree of flooding we investigated the σ_0 values for the following flooding states: 'open water', meaning free water surfaces with negligible vegetation protruding through the water surface; 'flooded' areas, with vegetation protruding through the water surface, enabling a high backscatter of the radar signal; and 'not flooded' areas. On three wet season (Dec '06, early Sept '07, late Sept '07) and three dry season (Feb '07, Mar '07, May '07) images, two to five polygons were defined in each image for each flooding state and analyzed for mean and standard deviation of σ_0. Polygon size ranged from 340 to 30,230 pixels (median: 1,370 pixels). Similar techniques were used by Hess et al. (2003) and Martinez
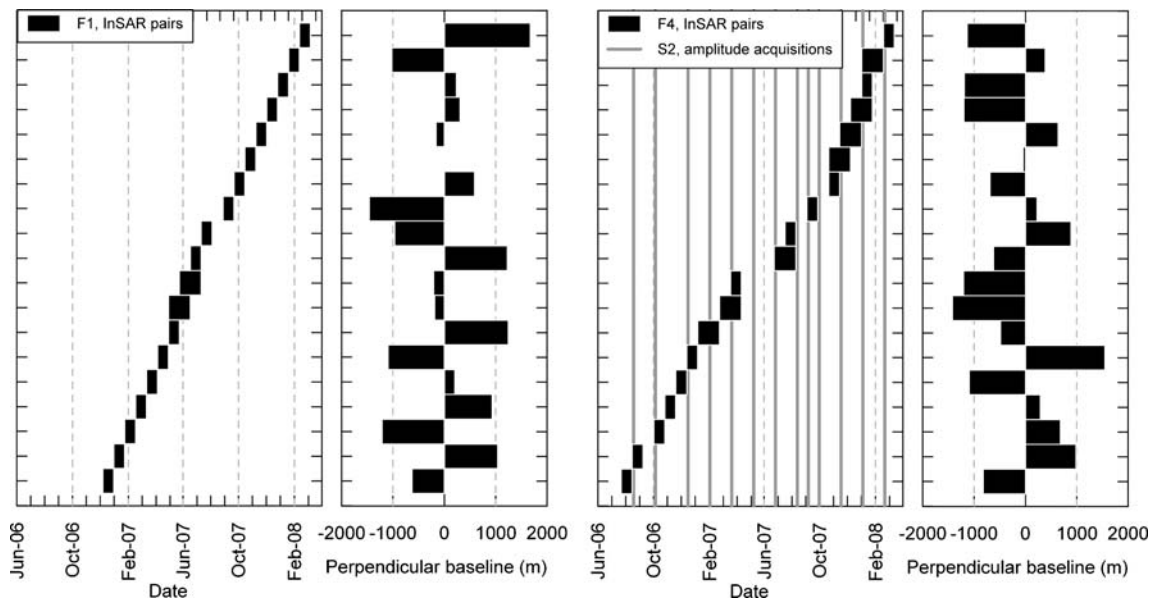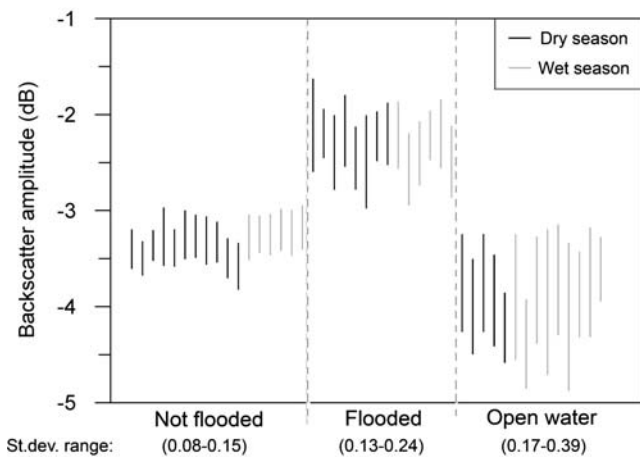
Fig. 2 InSAR image pairs, with their acquisition times, time spans and perpendicular baselines, for RADARSAT-1 F1 and F4 tracks, respectively. Acquisition times for RADARSAT-1S2 track, used for amplitude analysis, also shown

and Le Toan (2007). Since no ground truthing data were available, aerial photos, Landsat, and QuickBird images were used to confirm that polygons belonged to the different flooding categories. In Fig. 3, we indicate 95% confidence intervals for the σ_0 values, calculated for each polygon in each image, along with the standard deviation ranges of σ_0 for each category.

Clearly, both backscatter amplitudes and standard deviations are different for flooded and dry areas (Fig. 3). Values of σ_0 larger than −2.9 dB indicate flooded areas, whereas dry pixels have lower σ_0 values. It is however also obvious that the groups had some overlap. A Kruskal-Wallis H test

indicated statistically significant differences among the three classes ($\chi^2=39.0$, $p<0.001$). Multiple comparison test using Scheffé's method showed that all three classes were significantly different ($P<0.05$). Based on the analyzed σ_0 values we chose the class thresholds shown in Table 1, using a stringent approach to avoid overlapping values. We included the 'unknown' category to accommodate for the overlap between 'not flooded' and 'flooded' categories.

The 'not flooded' and 'open water' groups, in particular, had a large overlap in σ_0 values; yet a clear difference in the standard deviations of open water and non-flooded pixels was evident (Fig. 3). Therefore, we calculated images of backscatter standard deviation using a 9×9 pixel window, and used these images to refine the classification, so that pixels with backscatter < -3.2 dB and standard deviation > 0.17 were also classified as open water. The blue 'open water' category and the dark green 'not flooded' category in Fig. 4 are the ones distinguished by standard deviation differences. The window size used for standard deviation calculations was optimized by trial-and-error.


Fig. 3 Ninety-five % confidence intervals for the mean backscatter amplitude of polygons in both dry and wet season images for three different flooding states

Table 1 Classification criteria for backscatter amplitude (σ_0). Final classification also used differences in backscatter standard deviation to differentiate open water and not flooded areas

	Open water	< -3.8	dB
-3.8 dB $\leq$	Open water or not flooded	≤ -3.2	dB
-3.2 dB $<$	Not flooded	< -3.0	dB
-3.0 dB $\leq$	Intermediate/unknown status	≤ -2.9	dB
-2.9 dB $<$	Flooded		
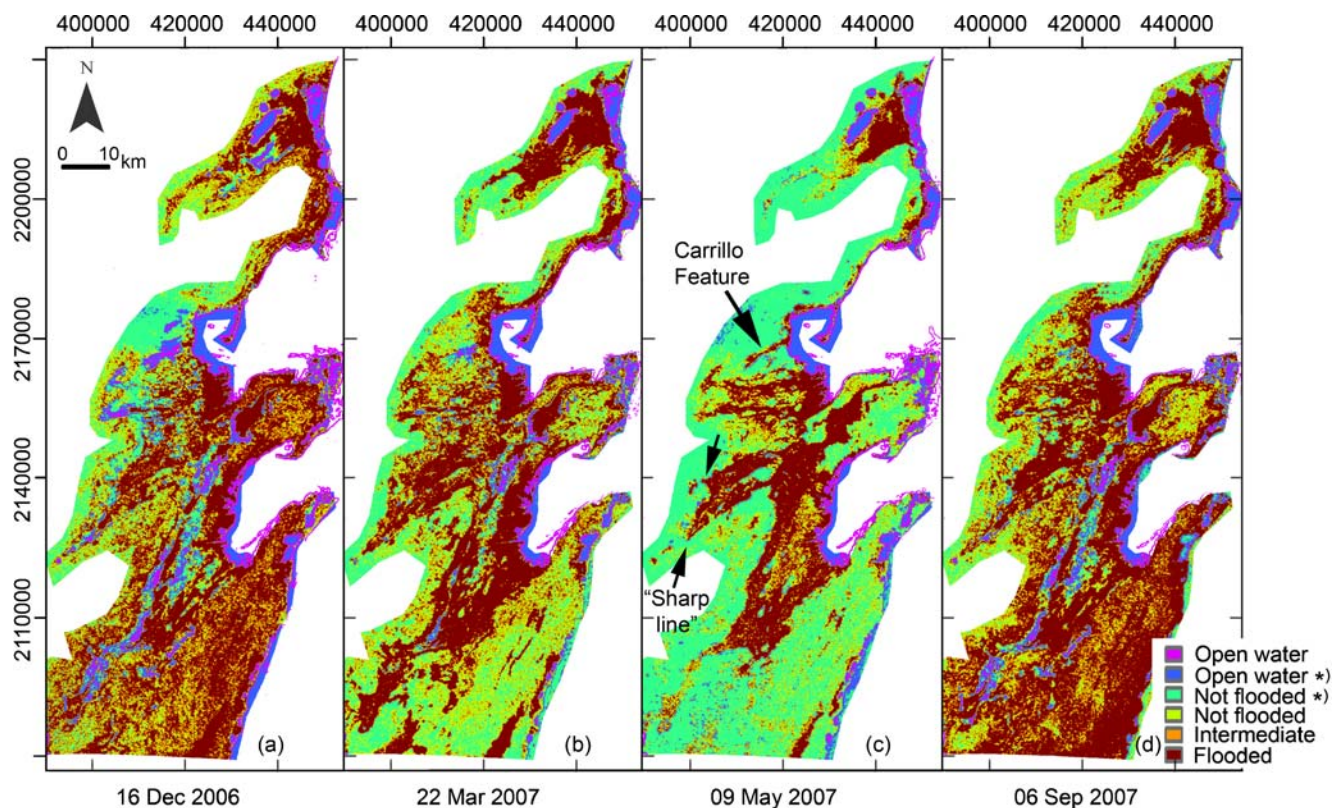
Fig. 4 Examples of flooding maps created from SAR backscatter amplitude images. **a** maximum flooding extent when no hurricane has passed, **b** a normal medium flooding extent example, **c** minimum, and **d** maximum flooding extent in the time series analyzed. Rough mask applied to disregard surrounding forest and ocean values. *Arrows* indicate the location of the Carrillo Feature and the sharp line west of the Tigritos slough. *indicates classes differentiated using standard deviation differences

InSAR Data and Analysis

The InSAR technique is well established for measuring surface displacement due to tectonic deformation (e.g., Massonnet et al. 1993) and glacier motion (e.g., Goldstein et al. 1993). Its application for wetland hydrology has only recently been recognized (Alsdorf et al. 2000). Interferograms are created by using two SAR images with nearly identical viewing geometries, co-registering them and subtracting the phases of the images for each pixel. Alsdorf et al. (2000, 2001, 2007) and Wdowinski et al. (2004, 2008) used L-band data for their interferograms over wetlands. Lu et al. (2005) and Kim et al. (2005) showed that C-band data are also useful for wetland interferometry over herbaceous wetlands. Kim et al. (2005) found that RADARSAT-1 data in particular maintain a good coherence over short time intervals due to their polarization (HH), which penetrates vegetation more easily, and due to the large incidence angle and high resolution of the Fine Beam modes. RADARSAT-1 data are advantageous for wetland InSAR due to the short orbit repeat cycle of 24 days because interferograms with short time spans can be constructed, so that coherence is more easily maintained over the often highly dynamic wetland surfaces.

We used RADARSAT-1 Fine Beam F1 and F4 modes data for the interferograms. Nineteen interferograms were formed with each of these tracks, covering the time interval July 2006 to March 2008. Image acquisition dates, time spans and perpendicular baselines are seen from Fig. 2. We used the ROI_PAC software (Buckley et al. 2000) to generate interferograms. Topographical phase was removed using the Shuttle Radar Topography Mission (SRTM) 3 arc-second digital elevation model. Based on the topography and baseline relation (Zebker and Villasenor 1992 – Eq. 25), and using perpendicular baselines of 800–1,500 m and slant range of 1,000 km, a 4–9 m topographic error will cause phase errors between 0.009 and 0.042 radians. This is negligible compared to the observed phase changes (1–7 phase cycles of 0 to 2π).

The resulting interferometric phase (φ) varies between $-\pi$ and $+\pi$. Unwrapping of the phase was done with the GZW algorithm (Goldstein et al. 1988), thus converting cycles of 0 to 2π to continuous surfaces of 0 to $n*2\pi$, where n is an integer depending on how many cycles ('fringes') follow each other.

We did not apply the spatial interferogram filtering typically used to improve interferogram quality, since we found that this smoothes out important densely spaced

fringes that characterize the Sian Ka'an interferograms. To resolve this type of fringes we needed as high a spatial resolution as possible. For the same reason, use of "multilook" processing, a standard signal-averaging procedure used to further reduce phase noise in interferograms, was minimized. Resulting resolution of our interferograms was 18 by 23 m (ungeocoded), and 58 by 61.5 m (geocoded to UTM, zone 16, WGS84 datum). Both were used in the image analysis.

The unwrapped interferogram phases (φ) were recalculated to water level changes (Δh) using the wavelength (λ) and incidence angle (θ, in radians) of each beam through the following formula, while assuming that all range changes are caused by vertical displacements only:

$$\Delta h = -\frac{\lambda \varphi}{4\pi \cos(\theta)} \qquad (1)$$

For F1, $\theta = 38.5°$ whereas for F4, $\theta = 44.5°$ (RADARSAT International 1995), hence one phase cycle of $0-2\pi$ corresponds to 3.6 cm (F1) and 3.9 cm (F4) vertical displacement, respectively.

Results and Discussion

Flooding Extent as Determined from SAR Data

Within the investigated time interval, classification of the SAR amplitude images showed that the flooding extent in Sian Ka'an varied between 1,067 km^2 and 2,588 km^2 (mean: 2,030 km^2), when we totalled the area of 'flooded' and 'open water' pixels (Figs. 4 and 5). Of the pixels located within the official boundary of Sian Ka'an, between 25% and 48% (mean: 39%) were flooded during the year. This fits well with accounts that the wetlands take up roughly $^1/_3$ of RBSK's area (Olmsted and Duran 1990). The smallest flooding extent occurred at the end of the dry season (May 2007, Fig. 4c) whereas the largest extent occurred after Hurricane Dean (September 2007, Fig. 4d). In the year without extreme rainfall from hurricanes, the largest flooding extent occurred in December 2006, about 2 months after the end of the rainy season (Fig. 4a). Figure 4b is an example of medium flooding extent (March 2007).

We assessed the accuracy of the flooding maps by comparing them with processed Landsat ETM+ imagery. No Landsat data with sufficiently low degree of cloud cover were available for the exact SAR acquisition dates used. The closest date was 05 December 2007 (0–1% cloud cover), which was compared with the flooding map of 17 November 2007. Two Landsat scenes (path 19/row 46 and path 19/row 47) were used to cover the study area. We used an unsupervised classification (using the ER Mapper
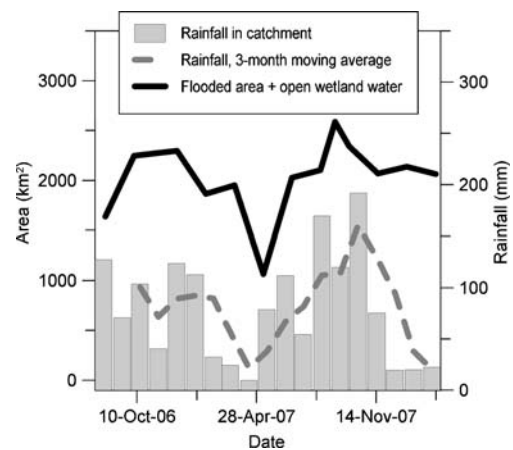
Fig. 5 Variations in flooding extent with time, as derived from classification of SAR imagery. Precipitation data (*histogram*) from the Tropical Rainfall Measuring Mission (TRMM, NASDA/NASA 2008), along with a 3-month backward moving average of this precipitation (*thick dashed line*). These data are a spatial average for the topographical catchment of Sian Ka'an (defined in Neuman and Rahbek 2007)

software) on the thermal infrared bands 6L and 6H and the mid-infrared band 5, combined. The thermal bands yield information about soil moisture whereas band 5 generally provides information about soil and plant moisture content (USGS 2003). We also calculated normalized difference vegetation index (NDVI) from the Landsat data as: (NIR−red)/(NIR + red), where 'NIR' is the near-infrared band 4 and 'red' is band 3. Negative NDVI values can either indicate water, snow (not applicable), or clouds (< 0.4% in scene row 47, 0% in scene row 46). We therefore used negative NDVI to identify 'open water'.

We classified 85% of our SAR flood maps' open water area as open water in the Landsat data. For the combined categories of 'flooded' and 'open water' the agreement was 63%, and for 'not flooded' pixels, agreement was 75%. Twenty-four percent of the area classified in the SAR flood maps had missing values in the Landsat images, since the instrument was operated in SLC-off mode. The percentages of agreement only considered pixels defined in both types of images. Considering that the two datasets were 18 days apart, the overlap in classifications between the Landsat classes and the SAR flood maps is satisfactory, and is in agreement with other studies (e.g., User's accuracies range from 65–95% in Hess et al. 2003 and 56–80% in Bourgeau-Chavez et al. 2005).

InSAR Images

Generally interferometric coherence was high over wetlands, whereas it was very low over forest areas, which means that the InSAR technique worked well over the Sian Ka'an wetlands. Between 78% and 91% of the area within

the wetland mask was coherent in the produced interferograms. The high degree of coherence was partly attributable to the short time spans used. In contrast, a dry-season/wet-season interferogram could not be formed for the area, probably due to decorrelation over time, since the surface characteristics varied extensively, as exemplified by the flooding maps (Fig. 4). The degree of coherence is also related to the radar wavelength used compared to the dimensions of the dominant vegetation. Temporal changes in vegetation due to growing season were considered to have negligible influence on the coherence, since dominant vegetation was evergreen mangrove, perennial grasses, and sedges, with no leaf-off season.

Interferograms produced over Sian Ka'an were sometimes smooth, with few fringes and hence little relative water level change over the wetlands (Fig. 6b and e (wet season), Fig. 6c (dry season)), and at other times have complicated patterns due to greater variations in the relative water levels (Fig. 6a and d). Mostly, the Sian Ka'an interferograms showed irregular fringe patterns. This was also found by Alsdorf et al. (2007) for the Amazon flood plains and by Wdowinski et al. (2008) for the unregulated part of the Everglades wetlands. Like Alsdorf et al. (2007) found for the Amazon floodplains, we saw in Sian Ka'an

that the smoothest interferograms patterns occurred at times when large water amounts occurred in the wetland, e.g., at the end of the rainy season in November and December (Fig. 6b and e). In contrast, the most irregular patterns were observed at the beginning and middle of the wet season, where surface water level changes were more localized (i.e., July–September). October had irregular patterns in 2006, while the patterns in October 2007 were smooth because hurricane Dean had recently provided large amounts of precipitation.

Interferogram fringes can be caused by water level changes in the wetlands, but can also be caused by atmospheric disturbances, topographical changes, and changes in the dielectric properties of the surface. The latter seems unlikely for the study area, and the topographic phase had been removed. Atmospheric disturbances at the latitudes of our study are mainly caused by large amounts of water vapor (clouds) in the local atmosphere that cause delay of the radar signal (Massonnet and Feigl 1998). An example of a fringe, which we attribute to atmospheric disturbances, is the circular pattern seen in the center of the interferogram in Fig. 6e. Kwoun and Lu (unpublished data, cited in Lu and Kwoun 2008) found 40–50% of interferograms over New Orleans to be influenced by atmospheric
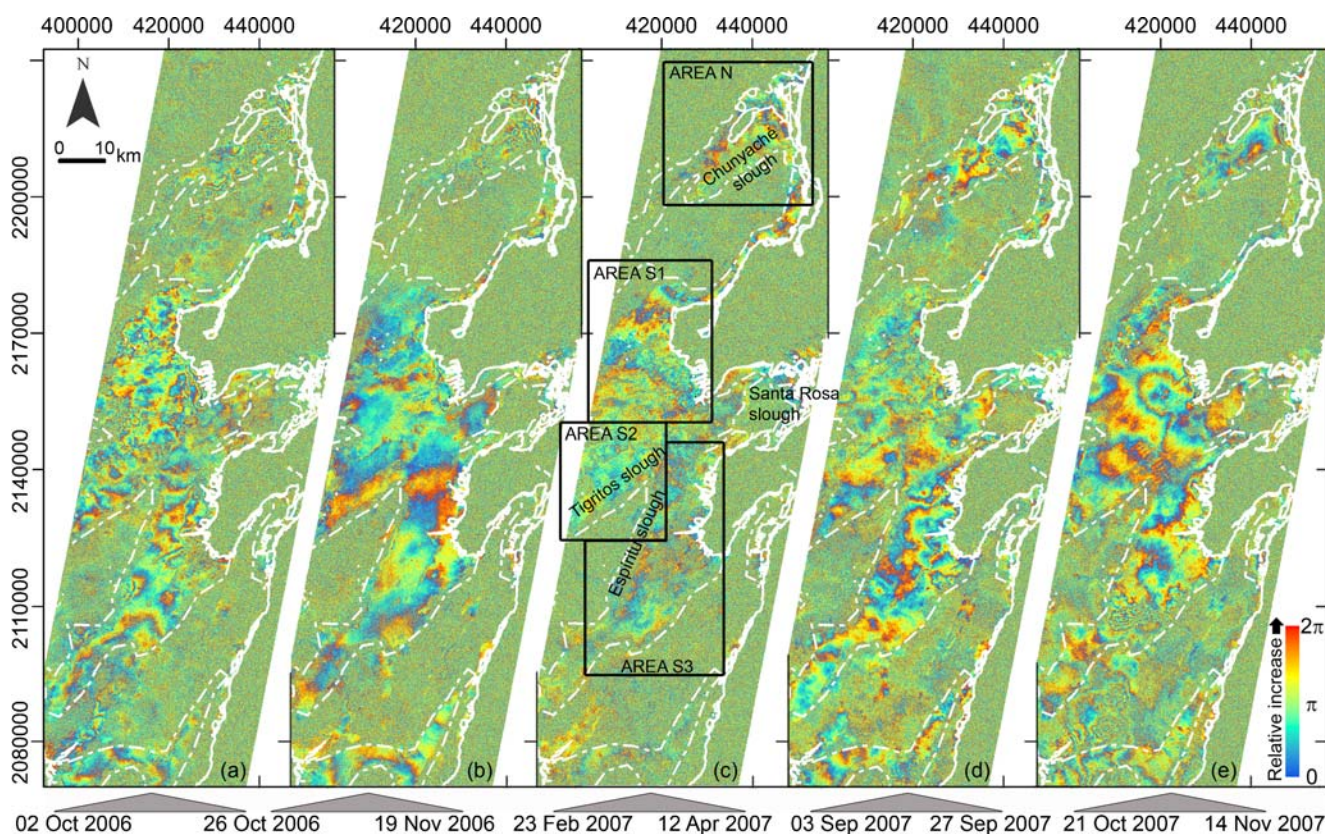
Fig. 6 Examples of the produced interferograms of the whole study area (Fine Beam F4), in the wet (**a**, **b**, **d**, **e**) and dry (**c**) season. Legend indicates direction of relative increase in water levels. *Full white line* is coast, *dashed white line* is the general outline of the wetlands. *Black boxes* show the location of the four different areas referred to in the text

delay patterns. Hence, in the analysis of our interferograms we only point out fringes and patterns that reoccur in the same places several times in interferograms that use different acquisitions, or patterns that can be associated with surface features such as tree barrier islands, channels etc.

Water Level Changes

Accuracy of InSAR-produced water level changes is usually derived by comparisons with *in situ* gauge height measurements. Gauge height measurements are also used to determine the offset between InSAR and absolute water level changes, transforming the relative InSAR changes to absolute changes (Wdowinski et al. 2008). Satellite altimetry can be used to measure absolute water levels over rivers, lakes, and wetlands (Berry et al. 2005). However, presently not enough suitable radar altimetry data are available over Sian Ka'an (R. G. Smith, Earth and Planetary Remote Sensing Laboratory, De Montfort University, UK, pers. comm. 2008).

We used our gauge height measurements to investigate the accuracy of the spatial pattern of water level changes obtained from InSAR. Table 2 displays water level changes as recorded on gauges and through interferograms (latest minus earliest date). We compared water level change differences between stations. Data were grouped in pairs of closest acquisition dates. There were 0–4 days difference in acquisition dates of InSAR and gauge height measurements. This should have negligible influence because water level changes varied slowly and smoothly where the gauges were located. InSAR water level changes between stations are within 0–2 cm of the gauge height measurements. Generally the InSAR data thus provide a good spatial representation of the water level changes.

Fringes in the interferograms relate to either local scale water divides or to water level changes, which are not spatially uniform. The latter can be caused by outflow,

accumulation of water if flow into an area is faster than flow out of it, and tidal changes. The largest relative water level changes take place in the four sloughs of Sian Ka'an (Chunyaché, Tigritos, Espíritu, Santa Rosa), and at four main coastal outlets of the wetlands (an area between Chunyaché slough and Caapechen lagoon, a trapezoidal area in Area S1, the mouth of the Santa Rosa slough, and the bays in Area S3)(see Fig. 6c for the locations of these features). Fringes at the four coastal locations may partly or fully be caused by tidal changes. Detected water level changes were up to 28 cm (seven fringes) within 24 or 48 days (Fig. 7). Maximum hydraulic gradient changes were: Area near L. Caapechen — 78 ppm; Chunyaché slough — 46 ppm; trapezoidal area — 49 ppm; Santa Rosa slough — 13 ppm; mouth of Santa Rosa slough — 65 ppm; Tigritos slough — 8 ppm; Espíritu slough — 10 ppm; and bays in Area S3 — 117 ppm. Changes were thus 7 – 117% of the hydraulic gradient measured in the natural channel.

Timing of Sian Ka'an's Main Water Input

Catchment rainfall distribution during the time interval for the created flooding maps (Fig. 5) showed that flooding extent was related to the amount of rainfall. Interestingly, a 3-month backward moving average of the catchment rainfall data produced a pattern very similar to the flooding extent pattern (Fig. 5), which indicated that the flooding dynamics result from averaging and delaying the catchment response, and suggested that Sian Ka'an is indeed fed by ground water from a catchment larger than the area of the reserve itself. Water travel time from the catchment appears to be on the order of 3 months. Minimum flooding extent occurred slightly later than the minimum on the moving average curve, and might be explained by lower hydraulic gradients and slower ground-water flow during the dry season. Yet, not only the amounts of rain, but also the intensity of the rainfall influenced the extent of the wetland flooding. Hence, the

Table 2 Water levels change differences between gauge stations Muyil and Xlapak, derived from gauge height measurements and InSAR data. Gauge heights only read to nearest cm, hence no decimal places. As a rule of thumb, relative spatial accuracy of InSAR measurements is $^1/_{10}$ cycle, i.e. approx. 0.4 cm with the data used in this study

	Date (in 2007)	Diff. (cm) Muyil-Xlapak	Diff. (cm) Xlapak-Termite	Diff. (cm) Termite-Km7
Gauge heights	21Mar-10Apr	−1	*	*
InSAR data	19Mar–12Apr	−0.8	*	*
Gauge heights	29Apr–26May	0	*	*
InSAR data	30Apr–24May	0.1	*	*
Gauge heights	25May–10Jul	−1	*	*
InSAR data	24May–11Jul	0.5	*	*
Gauge heights	17Jun–07Jul	−2	3	−1
InSAR data	17Jun–11Jul	−1.4	1.1	−0.8

*Not presented due to lack of stage data
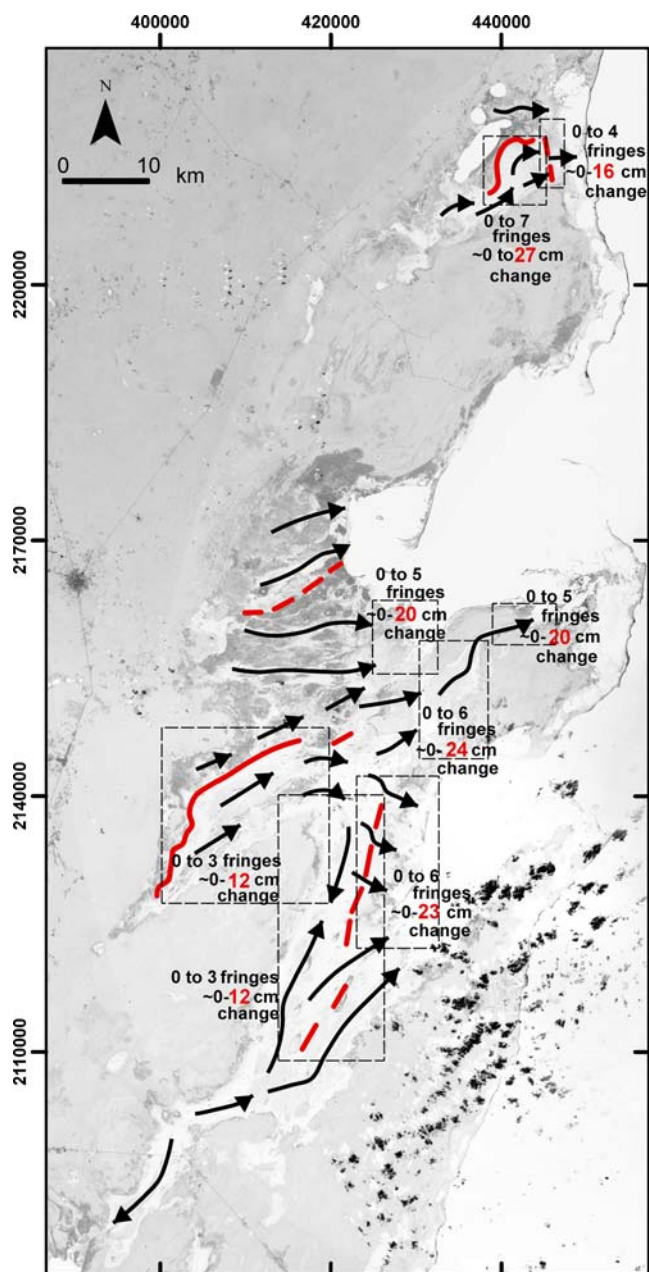
Fig. 7 *Black arrows*: Surface water flow directions, deduced from interferograms and visual inspection of Landsat imagery. *Red lines*: Semi- or impermeable water divides, deduced from abrupt phase changes and fringe lines. *Dashed boxes*: Areas with largest water level changes (most fringes). Background image: Grey-scaled Landsat TM Tri-Decadal mosaic, band 7

largest flooding extent occurred after an extreme rainfall event (the hurricane) and not after the largest amount of rain had fallen within the catchment (October 2007).

The smooth fringe patterns described for interferograms indicated that Sian Ka'an had the largest amounts of surface water in October, November, and December, as also indicated by the flood maps. Data from two ground-water hydrographs supported this finding. In Presidente Juarez,
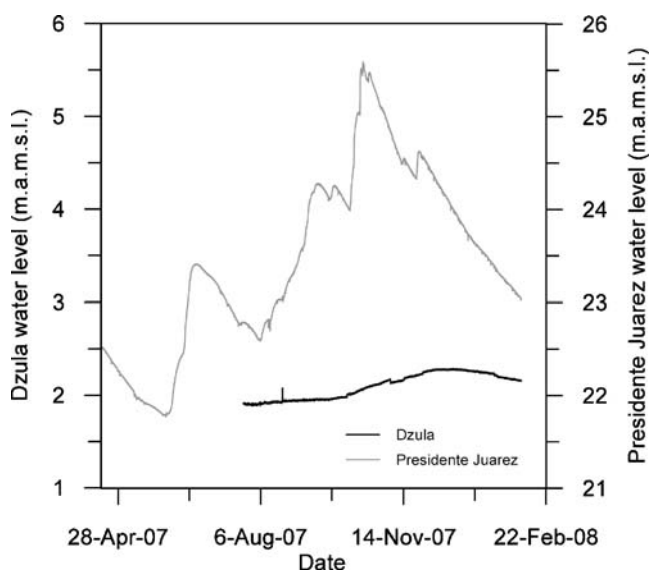
ground-water levels in a perched aquifer had their maximum in October 2007, whereas in Dzula, ground-water levels, measured in the regional aquifer, peaked in November–December 2007 (Fig. 8, locations shown in Fig. 1). Possibly the regional aquifer is partly recharged by the perched aquifer, which may explain the difference in timing of the maxima in the hydrographs.

Main Inflow Areas

Although the ground-water sources for the Sian Ka'an wetlands are diffuse, the flooding maps and interferograms revealed features from which we might deduce information about main water input zones to the wetlands. Below we propose three main water input areas, based on analysis of the SAR and InSAR data.

The flood map of the driest acquisition (Fig. 4c) indicates areas with main water input because areas still flooded during the peak of the dry season probably receive water from permanent input sources. The Tigritos slough (Area S2), the Chunyaché slough (Area N), and three channel-shaped flooded areas in Area S1 were flooded even at the driest times of the year. We therefore propose that these are main water input areas to Sian Ka'an.

The Tigritos slough always had water and high coherence east of a sharp line at the western end of the slough running SSW-NNE (Fig. 4c). Shapes of tree islands, seen in Landsat imagery, showed that the slough's predominant surface water flow direction is from west to east since the widest part of the teardrop-shaped tree islands indicates the upstream direction (Bazante et al. 2006). This suggests that the water source is at the western end. Likewise, fringes and tree islands in the Chunyaché slough showed that water flows

Fig. 8 Ground-water level changes in Presidente Juarez (perched aquifer) and Dzula (regional aquifer)

through the slough from west to east, indicating that the slough's source is located at its western boundary. In Area S1 the northern-most channel (named the Carrillo Feature in Fig. 4c) had dense fringes adjacent and parallel to it in a few interferograms (Fig. 9a), showing largest water level increase towards the feature and supporting the hypothesis that the feature feeds water into the surrounding wetlands.

The so-called Rio Hondo fault system is a series of sub-parallel normal faults, trending SSW-NNE (approx. N30E) (Weidie 1985). Some have their surface expression in the fault-guided lakes seen southwest of Sian Ka'an, of which the largest is Laguna de Bacalar (Fig. 10). The Rio Hondo faults may extend as far north as the northern part of Sian Ka'an (Weidie 1985), although no detailed maps of the location and extent of these faults exist. The Holbox fracture system, also trending SSW-NNE (approx. N5-10E) is located north of Sian Ka'an. Its southern terminus is not well determined, but possibly the Holbox and Rio Hondo fault systems intersect (Southworth 1985). Faults are known to guide the shape of the coast in the study area. The permanent water sources of Sian Ka'an proposed above may be connected to these fault systems. Based on geochemistry, Perry et al. (2002) established that Laguna de Bacalar does not have a direct hydrological connection to the ocean despite its proximity to the sea. We propose that the Rio Hondo fault system instead may be hydrologically

connected to Sian Ka'an. The surprisingly linear western boundary of the Tigritos slough suggests that this slough may be fed by a ground-water-bearing fault. When this line is extended, it touches the most upstream point of the Carrillo Feature (Fig. 10). This line is parallel to the fault-guided coastline north of Sian Ka'an and the Holbox fracture system. Additionally, a line can be drawn following both the western edge of the depression forming the Area S2 wetlands and the ends of the two other permanently flooded channels in Area S1 (Fig. 10). This line parallels the coast at the bays and at the southern Mahahual Peninsula. Finally, the western edge of Chunyaché slough's permanently flooded part parallels the Holbox fracture zone as well as the series of lakes located on this line (Fig. 10).

Flow Directions and Local-Scale Water Divides

Water flow directions within the Sian Ka'an wetlands have not previously been described. InSAR data, combined with visual inspection of Landsat imagery, reveal flow paths, wetland dynamics, and local-scale water-divides. Figure 7 depicts dominant overall surface water flow paths within Sian Ka'an, interpreted from InSAR data and Landsat imagery. Flow is assumed perpendicular to main fringe directions.

The interferograms showed adjacent areas, which had individually uniform water level changes, but between
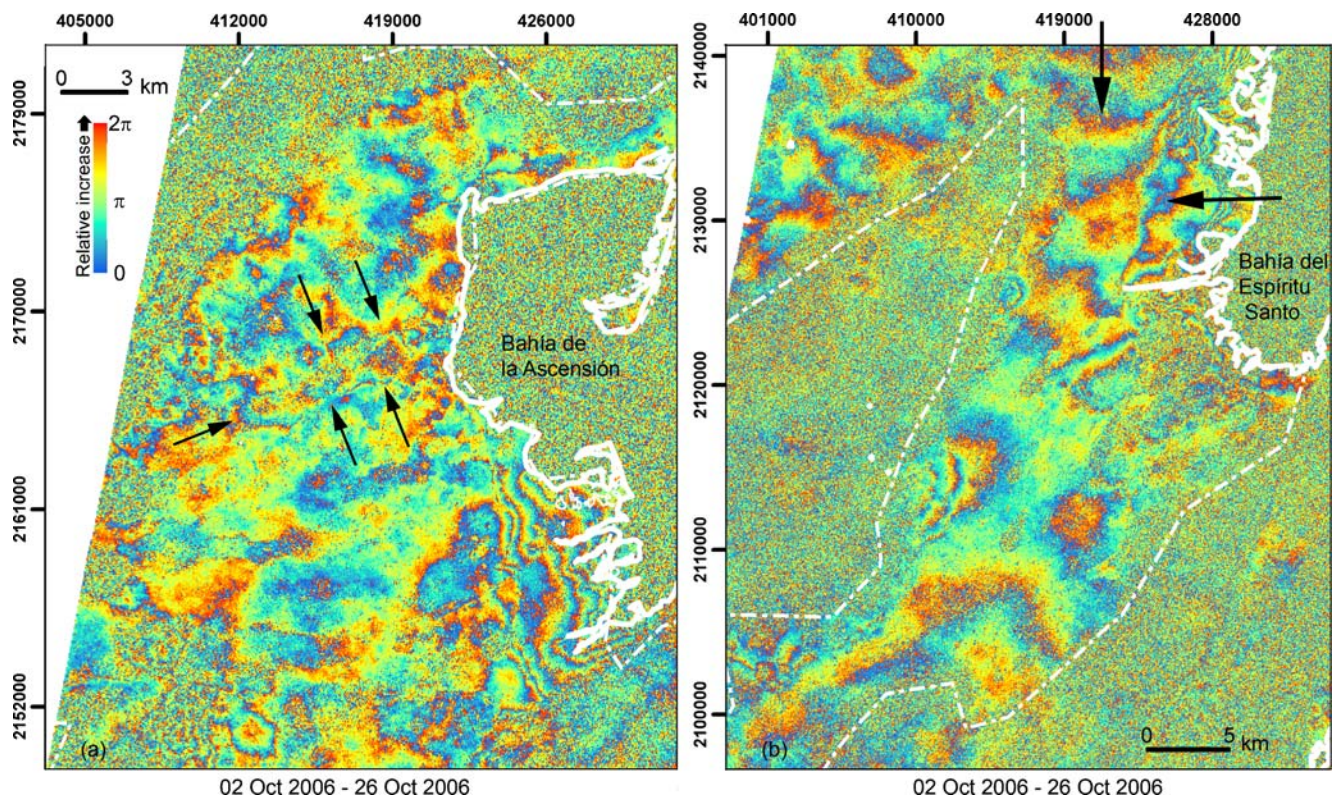
Fig. 9 a Interferogram over Area S1 with fringes parallel to the Carrillo Feature (arrows), and fringes in the trapezoidal area at the coast. b Interferogram over Area S3 showing that fringes in the Espíritu slough are normal to those in the bays area in the east (highlighted with arrows)

Fig. 10 The proposed faults as yellow lines, on the background of **a** Landsat TM Tri-Decadal mosaic, RGB: band 7, 4, 2; **b** topography data from the Shuttle Radar Topography Mission (SRTM) (grey-scale) and the May 2007 flooding map showing the smallest wetland extent. Color legend of the flooding map is seen in Fig. 4. Surface expression of the Rio Hondo faults are seen southwest of Sian Ka'an as elongated water bodies in (**a**) and depressions in (**b**). The Holbox fracture zone is partly seen in (**b**) as a line-shaped depression north of Sian Ka'an
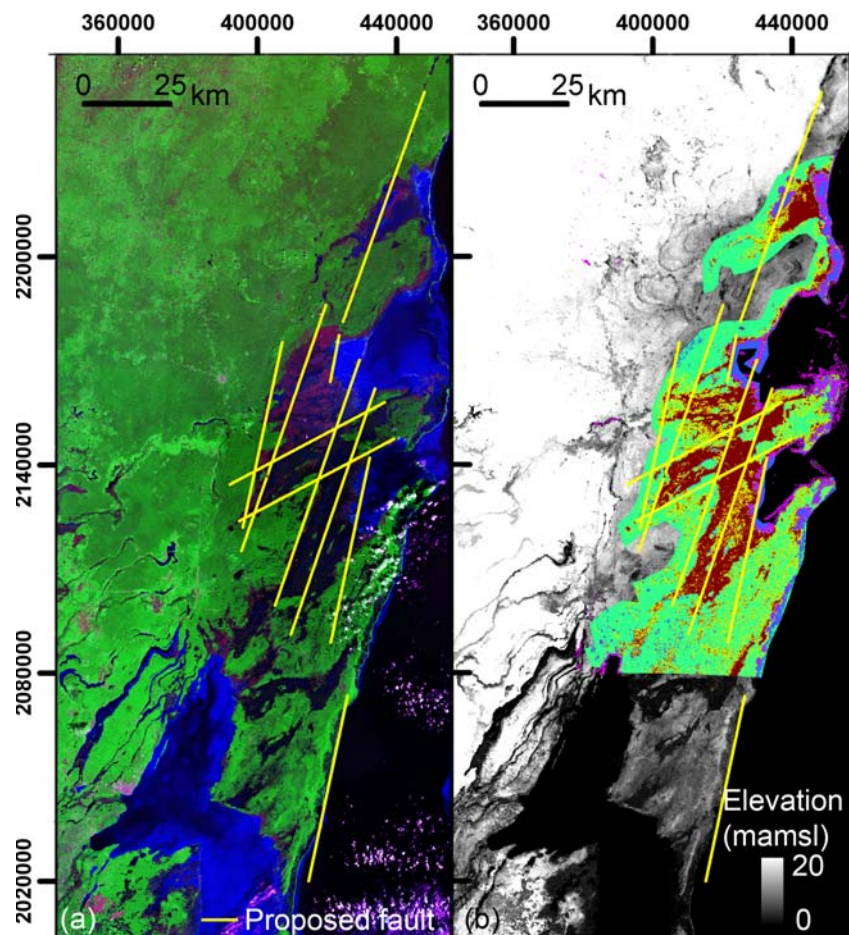
which there was a sharp change in phase. Such features are interpreted as local scale water divides (red lines on Fig. 7). These divides may not be impermeable for water. The flooding regime however differs on each side of the divides. The divides may be caused by differences in

vegetation cover (influencing the hydraulic resistance) and/ or topographical relief (determining the flow direction).

The divide in Area N traces the boundaries of the Chunyaché slough (Fig. 11a and b). Part of the divide, sub-parallel and close to the Chunyaché lakeshore, had trees visible
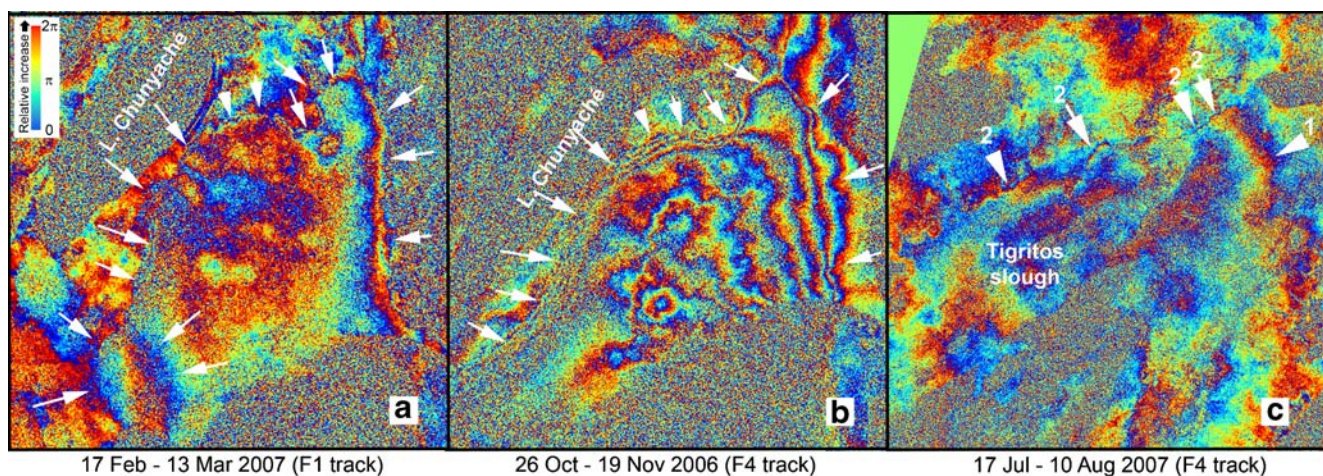
Fig. 11 a and **b**) Interferograms over the Chunyaché slough in Area N. *Arrows* highlight the fringes outlining the slough (**a** + **b**), and where it widens at the slough's western narrow part in (**a**). Many fringes within the slough are seen in (**b**), perpendicular to the flow

direction. **c** Interferogram over Tigritos slough of Area S2. Arrow "1": Fringes indicating eastward flow direction from Tigritos to Santa Rosa slough. Arrows "2": Fringes indicating the divide between the outflow from the Tigritos slough and the area just north of this slough

on QuickBird imagery (Google Earth) indicating slightly higher topography here. Thus this water divide may be caused by minute differences in topography, which cannot be seen on the Shuttle Radar Topography Mission digital elevation model (SRTM DEM). Like other wetlands in low-relief landscapes (e.g., Everglades, Leonard et al. 2006; Okavango Delta, Gumbricht et al. 2005), water movement in Sian Ka'an is thus influenced by microtopography, which cannot be resolved by existing elevation models of the area.

The Tigritos slough was in many interferograms outlined by an abrupt phase change, or one or several fringes (e.g., Fig. 11c). At times of high water the boundary was somewhat further out, making the slough larger. The Tigritos slough's northern and southern boundaries are strikingly linear, and may also be fault guided (Fig. 10). At the slough's outlet, the water flow is partly directed towards the south and Area S3, and partly towards the east and the Santa Rosa slough (Fig. 7). This was supported by fringe directions (e.g., Fig. 11c) as well as the shape of tree islands seen on Landsat imagery. The change in flow direction could result from a tilt in topography, possibly caused by a fault forming the very linear western edge of the Espíritu slough (Fig. 10).

The fringe direction of the Espíritu slough and the bays near Bahía del Espíritu Santo were perpendicular to each other (Fig. 9b). This indicates an interesting flow pattern, bending off from a north–south direction in the slough to a west–east direction near to the bays. We suggest that this flow pattern is caused by a fault-induced tilt in topography at the eastern boundary of the slough (Fig. 10), yielding a steeper topographical gradient towards the bays.

Conclusions

Analysis of SAR and InSAR data over the Sian Ka'an wetlands showed that these remotely sensed data yield valuable information about this vast ground-water-fed wetland, for which hydrologic and hydrodynamic information is hard to obtain. Classification of SAR backscatter amplitude yielded time series of flooding extent maps, which can be used to calibrate hydrologic surface water models. Comparing these maps with catchment rainfall variations can give an order-of-magnitude estimate of ground-water travel time from the catchment to the wetlands.

Interferograms and flooding maps showed that sloughs are main water input areas, possibly fed by water-filled faults acting as main ground-water-transportation pathways. This has implications for protection of the wetlands, since transport of pollutants through such higher-permeability zones must be taken into account when planning and managing land use in the catchment of Sian Ka'an.

We found that information on water divides and flow directions can be obtained from interferogram fringe patterns.

This type of information, or proxies for it (e.g., microtopography), is often difficult or impossible to obtain for vast wetlands. Therefore this new utilization of InSAR data, as well as the water level changes obtained, is valuable for correct hydrological modeling of wetlands. Moreover, the information can guide water quality monitoring programs, with the aim to identify pollution transport pathways. Flow directions are also important for further studies on the interaction between ecology and hydrology in the wetlands.

InSAR and SAR data add significant information to our knowledge of the hydrologic dynamics of Sian Ka'an that will be useful for better management of this internationally important wetland. The approach presented in the present paper may also be useful for investigating other ground-water-dependent wetlands.

References

Alsdorf DE, Melack JM, Dunne T, Mertes LAK, Hess LL, Smith LC (2000) Interferometric radar measurements of water level changes on the Amazon floodplain. Nature 404:174–177

Alsdorf DE, Smith LC, Melack JM (2001) Amazon floodplain water level changes measured with interferometric SIR-C radar. IEEE Transactions on Geoscience and Remote Sensing 39:423–431

Alsdorf D, Bates P, Melack J, Wilson M, Dunne T (2007) Spatial and temporal complexity of the Amazon flood measured from space. Geophysical Research Letters 34:L08402. doi:10.1029/2007GL029447

Bazante J, Jacobi G, Solo-Gabriele T, Reed D, Mitchell-Bruker S, Childers DL, Leonard L, Ross M (2006) Hydrologic measurements and implications for tree island formation within Everglades National Park. Journal of Hydrology 329:606–619. doi:10.1016/j.jhydrol.2006.03.011

Beddows PA (2004) Groundwater hydrology of a coastal conduit carbonate aquifer: Caribbean coast of the Yucatán Peninsula, México. Ph.D. Dissertation. University of Bristol, Bristol, UK

Berry PAM, Garlick JD, Freeman JA, Mathers EL (2005) Global inland water monitoring from multi-mission altimetry. Geophysical Research Letters 32:L16401. doi:10.1029/2005GL022814

Bourgeau-Chavez LL, Smith KB, Brunzell SM, Kasischke ES, Romanowicz EA, Richardson CJ (2005) Remote monitoring of regional inundation patterns and hydroperiod in the Greater Everglades using synthetic aperture radar. Wetlands 25:176–191

Buckley S, Rosen P, Persaud P (2000) ROI_PAC Documentation—Repeat Orbit Interferometry Package. Version 1.1. http://www.earth.ox.ac.uk/~timw/roi_pac/ROI_PAC_doc.pdf. Accessed 7 Mar 2008

Comisión Nacional del Agua (2008) Climate data 1952–2007 for the Yucatan Peninsula obtained from the database of Comisión Nacional del Agua, Merida, Mexico

Goldstein RM, Zebker HA, Werner CL (1988) Satellite radar interferometry—two-dimensional phase unwrapping. Radio Science 23:713–720

Goldstein RM, Engelhardt H, Kamb B, Frolich RM (1993) Satellite radar interferometry for monitoring ice-sheet motion—application to an Antarctic ice stream. Science 262:1525–1530

Gumbricht T, McCarthy TS, Bauer P (2005) The micro-topography of the wetlands of the Okavango Delta, Botswana. Earth Surface Processes and Landforms 30:27–39. doi:10.1002/esp.1124

Hess LL, Melack JM, Novo EMLM, Barbosa CCF, Gastil M (2003) Dual-season mapping of wetland inundation and vegetation for the central Amazon basin. Remote Sensing of Environment 87:404–428. doi:10.1016/j.rse.2003.04.001

Kim S-W, Wdowinski S, Amelung F, Dixon TH (2005) C-band interferometric SAR measurements of water level change in the wetlands: examples from Florida and Louisiana. Geoscience and Remote Sensing Symposium. IGARSS '05. IEEE International 4:2708–2710

Lang MW, Kasischke ES (2008) Using C-band synthetic aperture radar data to monitor forested wetland hydrology in Maryland's coastal plain, USA. IEEE Transactions on Geoscience and Remote Sensing 46:535–546. doi:10.1109/TGRS.2007.909950

Leonard L, Croft A, Childers D, Mitchell-Bruker S, Solo-Gabriele H, Ross M (2006) Characteristics of surface-water flows in the ridge and slough landscape of Everglades National Park: implications for particulate transport. Hydrobiologia 569:5–22

Lerer S (2008) Estimation of actual evapotranspiration using remote sensing data for the Yucatan Peninsula, Mexico. M. Sc. Thesis. Technical University of Denmark, Kgs. Lyngby, Denmark

Lesser JM (1976) Estudio hidrogeologico e hidrogeoquimico de la Peninsula de Yucatan. Proyecto Conacyt-NSF 704, Secretaria de Recursos Hidraulicos, Direccion de Geohidrologia y Zonas Aridas, Mexico

Lopez-Ornat A, Ramo C (1992) Colonial waterbird populations in the Sian Ka'an Biosphere Reserve (Quintana Roo, Mexico). Wilson Bulletin 104:501–515

Lu Z, Kwoun O (2008) Radarsat-1 and ERS InSAR analysis over southeastern coastal Louisiana: Implications for mapping water-level changes beneath swamp forests. IEEE Transactions on Geoscience and Remote Sensing 46:2167–2184. doi:10.1109/TGRS.2008.917271

Lu Z, Crane M, Kwoun O, Wells C, Swarzenski C, Rykhus R (2005) C-band radar observes water level change in swamp forests. EOS Transactions, AGU 86:141–144

Martinez J-M, Le Toan T (2007) Mapping of flood dynamics and spatial distribution of vegetation in the Amazon floodplain using multi-temporal SAR data. Remote Sensing of Environment 108:209–223

Massonnet D, Feigl KL (1998) Radar interferometry and its application to changes in the Earth's surface. Reviews of Geophysics 36:441–500

Massonnet D, Rossi M, Carmona C, Adragna F, Peltzer G, Feigl K, Rabaute T (1993) The displacement field of the Landers earthquake mapped by radar interferometry. Nature 364:138–142

Mazzotti FJ, Fling HE, Merediz G, Lazcano M, Lasch C, Barnes T (2005) Conceptual ecological model of the Sian Ka'an Biosphere Reserve, Quintana Roo, Mexico. Wetlands 25:980–997

Morales Barbosa JJ (1992) Los humedales, un mundo olvidado. Series: Sian Ka'an, Introducción a los Ecosistemas de la Península de Yucatan. Amigos de Sian Ka'an A. C.. Impresos MARCA, Mérida, Yucatán, Mexico

NASDA/NASA (2008) Tropical Rainfall Measuring Mission (TRMM), data product 3B43. TRMM algorithms were developed by the TRMM Science Team. TRMM data were processed by the TRMM Science Data and Information System (TSDIS) and the TRMM Office; archived and distributed by the Goddard Distributed Active Archive Center. TRMM is an international project jointly sponsored by the Japan National Space Development Agency (NASDA) and the U.S. National Aeronautics and Space Administration (NASA) Office of Earth Sciences

Neuman BR, Rahbek ML (2007). Modeling the groundwater catchment of the Sian Ka'an Reserve, Quintana Roo. Association for Mexican Cave Studies. Bulletin 18. AMCS bulletin publication

Olmsted I, Duran R (1990) Vegetación de Sian Ka'an. In: Navarro D, Robinson JG (eds) Diversidad biológica de la Reserva de la Biósfera de Sian Ka'an, Quintana Roo, Mexico. Centro de Investigaciones de Quintana Roo, Quintana Roo, pp 1–12

Perry E, Velazques-Oliman G, Marin L (2002) The hydrogeochemistry of the karst aquifer system of the northern Yucatan Peninsula, Mexico. International Geology Review 44:191–221

Pope K, Rejmankova E, Paris JF, Woodruff R (1997) Detecting seasonal flooding cycles in marches of the Yucatan Peninsula with SIR-C polarimetric radar imagery. Remote Sensing of Environment 59:157–166

Pozo de la Tijera C, Escobedo Cabrera JE (1999) Mamíferos terrestres de la Reserva de la Biosfera de Sian Ka'an, Quintana Roo, México. Revista de Biología Tropical 47:251–262

RADARSAT International (1995) RADARSAT illuminated—your guide to products and services. RADARSAT International Client Services, Richmond

Richards JA, Woodgate PW, Skidmore AK (1987) An explanation of enhanced radar backscattering from flooded forests. International Journal of Remote Sensing 8:1093–1100

Rio JNR, Lozano-García DF (2000) Spatial filtering of radar data (RADARSAT) for wetlands (brackish marshes) classification. Remote Sensing of Environment 73:143–151

Sass GZ, Creed IF (2008) Characterizing hydrodynamics on boreal landscapes using archived synthetic aperture radar imagery. Hydrological Processes 22:1687–1699. doi:10.1002/hyp.6736

Southworth CS (1985) Applications of remote-sensing data, eastern Yucatan. In: Ward WC, Weidie AE, Back W (eds) Geology and Hydrogeology of the Yucatan and Quaternary Geology of Northeastern Yucatan Peninsula. New Orleans Geological Society, New Orleans, pp 12–19

Ulaby FT, Dubois PC, van Zyl J (1996) Radar mapping of surface soil moisture. Journal of Hydrology 184:57–84

USGS (2003) Landsat: A global land-observing program fact sheet 023-03. http://egsc.usgs.gov/isb/pubs/factsheets/fs02303.html. Accessed 15 June 2008

USGS (2006) Shuttle Radar Topography Mission, 3 Arc Second, Finished 2.0. Global Land Cover Facility, University of Maryland, College Park, MD, USA. Accessed 15 June 2006

Wdowinski S, Amelung F, Miralles-Wilhelm F, Dixon TH, Carande R (2004) Space-based measurements of sheet-flow characteristics in the Everglades wetland, Florida. Geophysical Research Letters 31:L15503. doi:10.1029/2004GL020383

Wdowinski S, Kim S-W, Amelung F, Dixon T, Miralles-Wilhelm F, Sonenshein R (2008) Space-based detection of wetlands' surface water level changes from L-band SAR interferometry. Remote Sensing of Environment 112:681–696. doi:10.1016/j.rse.2007.06.008

Weidie AE (1985) Geology of Yucatan Platform. In: Ward WC, Weidie AE, Back W (eds) Geology and hydrogeology of the Yucatan and quaternary geology of northeastern Yucatan Peninsula. New Orleans Geological Society Publications, New Orleans, pp 1–12

Zebker H, Villasenor J (1992) Decorrelation in interferometric radar echoes. IEEE Transactions on Geoscience and Remote Sensing 30:950–959